Nanoscale

RSC Publishing

PAPER

View Article Online
View Journal | View Issue

Cite this: *Nanoscale*, 2013, **5**, 11776

Size-controlled fluorescent nanodiamonds: a facile method of fabrication and color-center counting

Remi Mahfouz,†[a] Daniel L. Floyd,†[b] Wei Peng,[a] Jennifer T. Choy,[b] Marko Loncar[b] and Osman M. Bakr*[a]

Received 28th June 2013
Accepted 24th September 2013

DOI: 10.1039/c3nr03320a

www.rsc.org/nanoscale

We present a facile method for the production of fluorescent diamond nanocrystals (DNCs) of different sizes and efficiently quantify the concentration of emitting defect color centers (DCCs) of each DNC size. We prepared the DNCs by ball-milling commercially available micrometer-sized synthetic (high pressure, high temperature (HPHT)) diamonds and then separated the as-produced DNCs by density gradient ultracentrifugation (DGU) into size-controlled fractions. A protocol to enhance the uniformity of the nitrogen-vacancy (NV) centers in the diamonds was devised by depositing the DNCs as a dense monolayer on amino-silanized silicon substrates and then subjecting the monolayer to He^+ beam irradiation. Using a standard confocal setup, we analyzed the average number of NV centers per crystal, and obtained a quantitative relationship between the DNC particle size and the NV number per crystal. This relationship was in good agreement with results from previous studies that used more elaborate setups. Our findings suggest that nanocrystal size separation by DGU may be used to control the number of defects per nanocrystal. The efficient approaches described herein to control and quantify DCCs are valuable to researchers as they explore applications for color centers and new strategies to create them.

Introduction

Diamonds possess outstanding mechanical robustness, chemical inertness, biocompatibility, and optical transparency over a broad range of wavelengths (200–2000 nm).[1,2] Moreover, diamonds can accommodate over 500 types of defect color-centers (DCCs), many of which are optically active, with long emission and spin coherence times, as well as thermally stable and resistant to photo-bleaching.[1] These characteristics of DCCs, combined with the properties of the host diamond crystal, have enabled the demonstration of many novel applications in metrology,[3] sensing,[4] super-resolution microscopy,[5,6] biolabeling,[7,8] magnetometry,[9] quantum computation, and quantum communications.[10–12] For example, the negatively charged and brightly emitting nitrogen-vacancy (NV) center, which is the most widely studied DCC in diamonds, has been used as a nanoscale NMR to map and sense magnetic spins in individual molecules,[4,13] a stable source of single photons at room temperature,[14] a highly sensitive temperature sensor, and a quantum qubit that can be manipulated with photons and magnetic fields.[15] The ability to control the placement and concentration of the DCC with respect to the specific nanostructure, such as a photonic cavity or a tip of a scanning probe, is essential for such applications.[16]

Although top-down approaches like focused ion-beam implantation[16–18] have succeeded in the placement of individual DCCs with nanometer precision within functional nanostructures in proof-of-concept devices, they remain challenging in terms of scalability and cost.

Alternatively, DCCs may be embedded in colloidally dispersed diamond nanocrystals (DNCs),[19,20] thereby combining the desirable properties of diamonds with the potential benefits of supramolecular nanoparticle chemistry. The surface of a DNC can be appended with various functional moieties and molecules[21–23] that provide an added dimension of molecular recognition and bottom-up-directed self-assembly.[24] Indeed, by tailoring the chemical interaction between the nanoparticle and specifically patterned patches on a substrate (*e.g.*, by conventional photolithography, soft lithography, or dip-pen nanolithography), researchers are able to control the placement of individual nanoparticles and of ensembles of nanoparticles on the substrate with nanometer precision.[25]

However, several challenges need to be overcome before such a scheme could become a viable way to direct the placement of DCCs on functional nanostructures. Ideally the DNCs have to be uniformly implanted such that each nanoparticle in the ensemble contains a similar and controllable DCC density (number per unit volume). In reality, studies have shown that

[a]*Division of Physical Sciences and Engineering, Solar and Photovoltaic Engineering Research Centre, King Abdullah University of Science and Technology (KAUST), Thuwal 23955-6900, Saudi Arabia. E-mail: Osman.Bakr@kaust.edu.sa*

[b]*School of Engineering and Applied Sciences, Harvard University, Cambridge, MA 02138, USA*

† These authors contributed equally to this work.

the density of DCCs is strongly and inversely correlated with the size of the crystal.[26–28] Unfortunately, as-synthesized DNCs (whether by detonation[29] or by high pressure high temperature (HPHT)[21,30]) have extremely broad size distributions.

Looked at from another perspective, this inverse correlation presents an opportunity to control the number of DCCs per particle by controlling the particle's size. Indeed, over the last several years, researchers have developed highly accurate methods to separate particles by size.[31] The most accurate of those methods is density gradient ultracentrifugation (DGU).[31,32]

Here, we demonstrate a facile scheme to prepare NV-containing DNCs in controlled-size fractions, and to efficiently quantify the density of their DCCs. We fabricated the DNCs by milling micrometer-sized HPTP diamonds and then separated them into size fractions by DGU. The nanocrystals were then deposited as a dense monolayer on specially treated silicon substrates, which enabled a uniform defect creation process upon helium-ion irradiation. Using a simple standard confocal setup, we quantitatively analyzed the ensemble of DNCs and identified a relationship between the particle size and the average number of NV defects per crystal. This relationship was in good agreement with results from previous studies that used more elaborate setups. Significantly, our results suggest size selection of nanocrystals provides a method to control the number of defects per nanocrystal. An efficient approach to control and quantify the concentration of DCCs will be useful to researchers in the diamond community as the number of interesting defects and ways to create them grow.

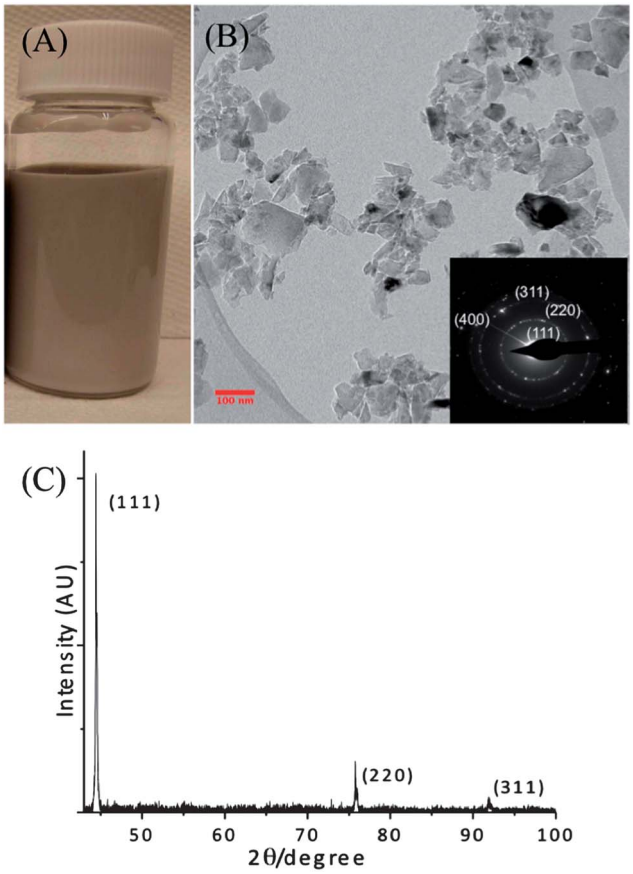

Fig. 1 (A) DNC dispersion in water, (B) a representative TEM image of a sample taken from the solution. Inset shows the selected-area electron diffractogram. (C) Powder XRD of the material dried from the DNC dispersion.

Results and discussion

DNCs were prepared on a large scale by ball-milling micron-sized synthetic HPHT diamond powder (210–250 μm).[30] HPHT diamond powder was chosen due its wide commercial availability, low-cost, high crystallinity and reasonably acceptable purity. Moreover, HPHT crystals are more amenable to the formation of NV centers of desirable optical and magnetic properties than are detonation nanodiamonds, another common diamond material. We modified the milling protocol to increase the yield of nanocrystals and streamlined the purification process by ensuring that only steel parts (balls and jar) came in contact with the diamond powder. All resulting steel impurities were easily removed by acid in a post-milling purification process. Previous publications have suggested that ball milling mixed with salt is an efficient method to reduce the size of the nanocrystalline particles and to increase the solubility of detonation nanodiamonds.[33,34] Hence, the diamond powder was further milled with NaCl and then dispersed in water after additional purification. The purified DNCs in solution are shown in Fig. 1A. It is worth noting that DGU requires relatively stable colloidal solutions of nanomaterials (*i.e.*, individually dispersed particles) to prevent aggregation, which would hinder the size separation.

Dried DNC samples were investigated by transmission electron microscopy (TEM), electron diffraction and X-ray diffraction (XRD). The microscopic investigations revealed that the samples consisted of highly faceted and irregularly shaped mono-crystalline DNCs less than 100 nm in size (Fig. 1B). Electron diffraction (inset, Fig. 1B) and XRD (Fig. 1C) studies of these powders indicated that the DNCs were only in the diamond cubic phase.

To study the formation of luminescent NV centers as a function of nanocrystal size, it was necessary to separate the polydispersed milled product (as shown in the TEM image in Fig. 1B) into fractions of narrower size distributions. The scientific literature contains a multitude of reports on fractionation methods that separate nanoparticles or nanotubes.[19,35,36] Specifically, to separate DNCs, multi-step centrifugation (*i.e.*, pelleting) is widely used because it is easy to perform with virtually any bench-top centrifuge.[19,37] Yet, this method is inherently flawed because the fractions collected at each step contain particles with various sedimentation coefficients due to the uniform dispersion of the particles throughout the entire centrifuge tube. A much more accurate approach is based on rate-zonal DGU (RZDGU), which also works by fractionating nanomaterials according to their varying sedimentation coefficients (which is related to the particle size).[33,36,38] This method avoids the varying length of the sedimentation path by layering the nanoparticle dispersion on top of a specially prepared density gradient (20% to 60% sucrose solutions in this

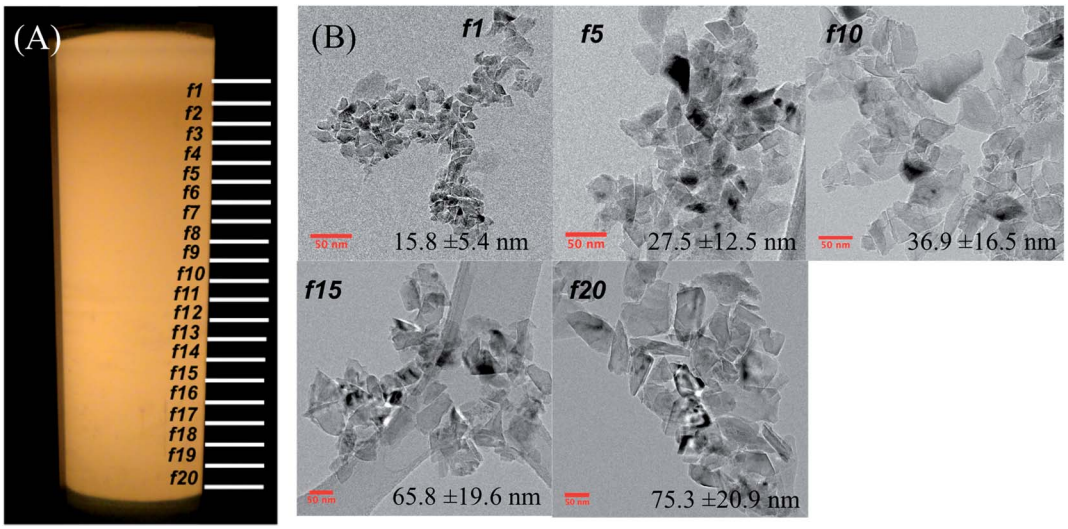

Fig. 2 (A) Image of a centrifuge tube containing DNC dispersion centrifuged in a density gradient. The resulting DNC fractions were collected and labeled depending on their position along the height of the tube. (B) TEM images of fractions f1, f5, f10, f15, and f20. The inset of each image shows the average size and standard deviation of the particles in each fraction.

work). Thus, sedimentation during centrifugation starts while all the nanoparticles are at nearly the same position with respect to the height of the tube, thereby decreasing the overlap of size distributions in neighbouring fractions. An additional advantage of RZDGU over pelleting is that all fractions can be collected after one centrifugation run, which largely increases the fractionation efficiency.

After layering on top of the gradient, the DNC dispersion was then subjected to centrifugation for enough time to allow the fastest sedimenting particles to traverse the centrifuge tube without reaching its bottom. Subsequently, the contents of the tube were collected into 20 fractions using a fractionator. An image of the DNCs gathered in the density gradient after centrifugation is presented in Fig. 2A. We chose fractions f1, f5, f10, f15, and f20 as candidates for further defect creation studies by irradiation (*vide infra*). The choice was made based on the sizes of the particles in these fractions, which were representative of all crystal sizes present in the tube. TEM images of the DNCs in the five fractions are presented in Fig. 2B (the average sizes and standard deviations of the DNCs in the images are marked correspondingly). The statistical data of these five fractions clearly indicated good size separation, considering the fact that RZDGU fractionation depends on the sedimentation coefficients of nanoparticles whereas size measurement by TEM depends on 2D projections of nanoparticles.[33] These five fractions were subsequently used in irradiation and optical characterization experiments.

Helium ion irradiation successfully and efficiently generated defects in DNCs.[18] Simulations indicate that a single He^+ with a few tens of keV energy can generate 20 to 40 vacancies compared to 0.1 to 10 generated by MeV electrons or protons.[39] The lower energy and dose allowed the use of inexpensive commercial implantation services (Innovion, Core Systems); however, the small penetration depth of He^+ at the available keV energy required that the diamond samples be deposited as thin films. We found that DNC fractions deposited by spin-coating on amino-silanized silicon formed dense monolayer films. The amino-terminated silicon promoted adhesion presumably by electrostatic interaction with the net negative charge on the diamond surface. Scanning electron microscopy (SEM; Fig. 3A) and atomic force microscopy (AFM; not shown) images of the spin-coated films confirmed that the DNCs were deposited as monolayers with minimal aggregation. Using these SEM images and the average crystal sizes determined from high-resolution TEM, we also calculated the nanocrystal density of each film to

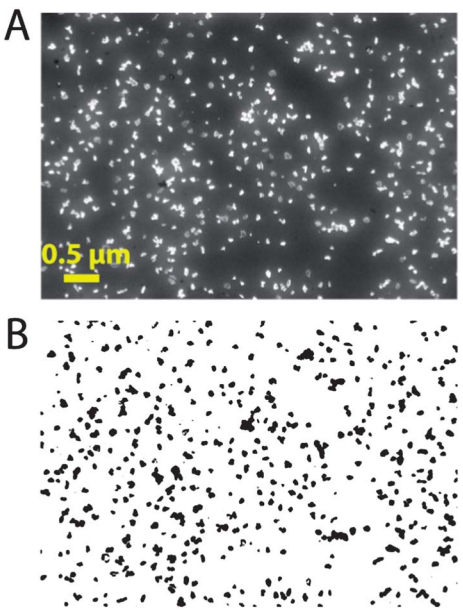

Fig. 3 (A) SEM image of fractionated diamond from layer 10 spincoated on an aminosilanized substrate. (B) Thresholded binary image from (A) used to determine the particle density.

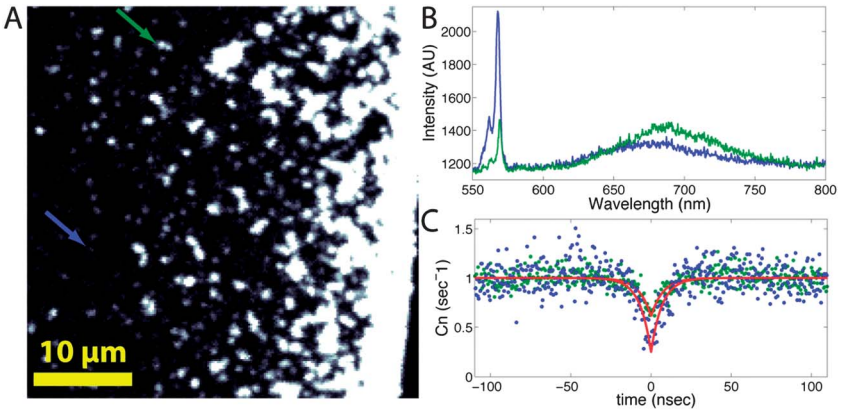

Fig. 4 Optical characterization of single NV luminescence. (A) Confocal 650–800 nm fluorescence image of drop-cast milled nanodiamond from f20 without irradiation. (B) and (C) Emission spectra and photon autocorrelation functions of NV centers within a focused laser spot placed in the regions indicated by arrows in (A).

permit comparison of photoluminescence data from each size fraction (Fig. 3B). The spin-coated DNC films were then irradiated with 20 keV He^+ and annealed at 800 °C for two hours under high vacuum (10^{-7} Torr) to form NV centers with intrinsic substitutional nitrogen present in the crystals. To minimize background emissions from graphite or other contaminants, the annealed samples were thermally oxidized at 465 °C for 30 minutes in pure oxygen.

Quantitative analysis of the NV content in diamonds is typically done by measuring the photon autocorrelation function, $g^{(2)}(t)$.[40] Because a single NV center can emit only one photon at a time, the $g^{(2)}(t)$ of a single NV center excited with a CW source exhibits antibunching behavior, $g^{(2)}(t) = 0$, with zero lag time. When more than one NV is present, the contrast at $g^{(2)}(0)$ diminishes as $g^{(2)}(0) = 1 - 1/N$, making it possible to quantify a small number of NV centers within the observed confocal spot. This approach is time consuming, however, and is not practical for characterizing the NV content of the milled DNCs described here, in which the number of NV centers is expected to vary considerably among individual nanocrystals. Instead, we used the intensity of the luminescence as a measure of the NV content by first measuring the photoluminescence count rate of a known number of NV centers using our confocal microscope (Fig. 4). The autocorrelation function was measured from regions of a sample containing DNCs with a low NV concentration, allowing the count rate per NV center to be estimated. Fig. 5A and B present confocal fluorescence images and emission spectra of the DNC films after irradiation and annealing. The variable apparent position of NV phonon sidebands in Fig. 4B and 5B are probably the result of emission from sp^2 carbon, which would most likely appear within the grain boundaries of fast sedimenting ND aggregates.[41] Additional defects, such as GR1, could also have been introduced during implantation.[42] Nonetheless, the PL intensities show a clear dependence on the average crystal size. After taking into account the film density and the NV emission rate, we calculated the average number of NV centers per nanocrystal for each sized fraction (Fig. 5C). The error associated with the data points in Fig. 5C is approximately 6% along the *y*-axis based on fluorescence measurements of $\sim 10^5$ particles and the standard error of two $g^{(2)}$ experiments to correlate NV number with fluorescence counts; while uncertainty along the *x*-axis ranges from ~30 to 50% according to the size distribution of each ND fraction as shown in Fig. 2.

The NV concentration we observed for all crystal sizes (<1 ppm) was substantially lower than the typical 200 ppm concentration of nitrogen in the HPHT diamond powder used in this study. Moreover, assuming that the actual number of color centers follows a Poisson distribution, we note that more than 63% of the ~37 nm nanocrystals contained no NV centers. To rule out the possibility that a failure in our sample preparation was responsible for the low NV yield, we performed the

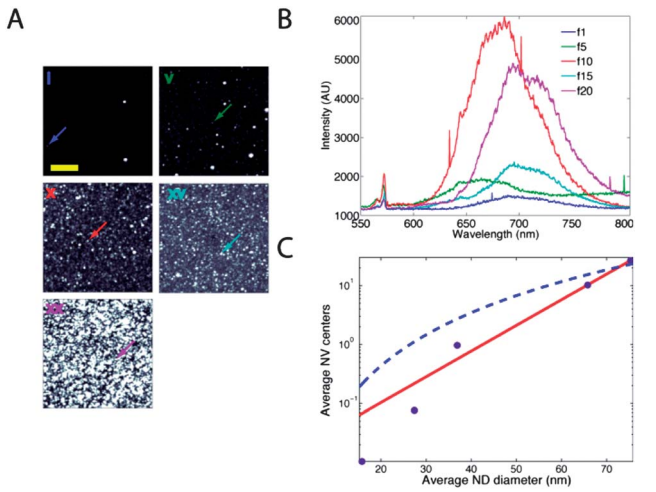

Fig. 5 Fluorescence characterization of irradiated nanodiamond films. (A) Confocal fluorescence images of f1, f5, f10, f15, and f20. The scale bar is 10 microns, and the image contrast is displayed from 0–5 × 10^4 counts per second. (B) Emission spectra from regions indicated by arrows in (A). Single peaks are the result of CCD detector noise. (C) The average NV content of nanocrystals as a function of size was estimated from the integrated luminescence intensity and nanodiamond film density. The error associated from each point is approximately 6% on the *y*-axis based on fluorescence from $\sim 10^5$ particles per image. The red solid curve is a least squares fit to $y = A\exp(-Bx)$, and the blue dotted curve is a fit to $y = Ax^3$.

same analysis on a sample of commercially purchased fluorescent DNCs (Academia Sinica) with an average crystal size of 35 nm that was prepared in a similar manner. We observed 0.96 NV centers per particle on average, which matches well with 0.97 NV centers in the 37 nm particles prepared in our study.

Photon autocorrelation analysis was previously used to demonstrate that the luminescence from tens of NV centers in electron- or proton-irradiated DNCs as small as 5 nm was stable. Other experimental and theoretical studies, however, showed that NV luminescence is unstable in small nanocrystals exhibiting intermittent blinking or quenching and is not formed efficiently due to the high probability of vacancies diffusing to the surface.[27,28,41] We confirm the latter results, suggesting that formation of stable NVs becomes increasingly rare, even after accounting for the nanocrystal volume (Fig. 5C, dotted curve). Instead, we observe a trend with better agreement with a thermodynamic model of NV formation and stability (Fig. 5C, red solid curve).[27] The discrepancy between these results and others[30,43,44] demonstrating large concentrations of NV centers is likely attributable to bias from selection of luminescent particles. Rather than selecting isolated luminescent DNCs for analysis, our method allows unbiased sampling of large ensembles of DNCs, including those with no NV centers, providing a far more accurate description of the NV content.

Conclusion

We have demonstrated a simple method for the preparation of fluorescent DNCs with controlled sizes using RZDGU and subsequent He^+ irradiation. Depositing the DNCs as a monolayer on a substrate enabled the creation of more uniform NV centers on all particles. We have devised an efficient technique to count the average number of NV centers per DNC. Optical studies performed on size-separated DNCs indicated a strong inverse correlation between the crystal size and NV concentration. Under the experimental conditions described in this work, DNCs around 37 nm in size contained on average about one NV center per particle. The number of NVs per crystal decreased dramatically at sizes below 37 nm and increased rapidly at sizes above 37 nm. Since the number of NV centers per particle can be mapped to the particle size, our work suggests that particle size separation can serve to control the number of defects within a crystal. Our future work will include studies of the size-dependent properties of other defect color centers in DNCs and of the chemical functionalization of the surface of the nanocrystals to enable bottom-up strategies for the placement and self-assembly of particles with specific number of color centers.

Experimental methods

Raw material and chemicals

The raw material used for our experiments was HPHT micron-diamond powder (Element six PDA999). The powder comprises crystalline synthetic diamonds with high impact strength, thermal stability and uniformly octahedral shapes in a size range of 210–250 microns and nitrogen at 200 ppm. Hydrochloride, perchloride, hydrochloric and nitric acids (Sigma Aldrich) were used to clean contaminants (iron and non-diamond carbon obtained during the ball-milling process) from the DNCs after milling. The DNCs were dispersed in MilliQ water (18 MΩ).

Milling

To convert the microdiamond powder into DNCs (<100 nm) in one simple and easy step, we used the ball-milling technique with hardened steel balls ($\phi = 5$ mm) in a 50 mL jar. A few grams (2 to 3 grams) of micron-diamond powder were mixed with 5 mL of MilliQ water and 70 g of hardened steel balls (approximately 1 : 30 diamond : balls) in the jar. The milling process was carried out following an optimized program: 1 hour of milling followed by a 30 minutes break for a total grinding time of 20 hours.

After milling, we obtained a viscous slurry of nanodiamonds contaminated by iron and carbon. We treated the slurry with HCl to dissolve the excess iron; the DNCs appeared to be gray after cleaning with MilliQ water. Afterwards, the DNCs were boiled with a mixture of acids (H_2SO_4 : HNO_3 : $HClO_4$) (1 : 1 : 1 v/v) at 120 °C for 1 hour under reflux. The DNCs turned white, which suggested that the non-diamond carbon and all other metal contents that had persisted after the HCl treatment had been removed. Finally, the particles were dispersed in MilliQ water and then centrifuged to form precipitates. The precipitates were collected and dispersed in water again. This rinsing procedure was repeated several times. The as-obtained particles were then dried for the subsequent salt-assisted milling procedure in which 300 mg as-obtained powders were mixed with 2.1 g NaCl and 50 g of steel balls in the jar and milled at 400 rpm for 15 h (1 h intervals with a 30 minutes break). The milled products were then dispersed in HCl solution to remove any iron contaminants. Finally, the particles were dispersed in water after the rinsing procedure.

Fractionation

A customized gradient station and a six-piston fractionator manufactured by BioComp Instruments Inc. (Fredericton, NB, Canada) were used in the fractionation procedure for preparing the density gradients and collecting the fractions, respectively. Centrifugation was carried out in a Thermo Scientific ultracentrifuge (WX Ultra 90) using a Superspin 630 rotor and Nalgene tubes (38 mL, Thermo Scientific).

We chose 20–60 wt% sucrose aqueous solutions to prepare the continuous density gradient. A 20 wt% sucrose solution was first laid at the bottom of the centrifuge tube up to the 45% level, with a 12 mL Norm-Ject syringe (Henke Sass Wolf) and a Vita 14 steel needle, and then a 60 wt% sucrose solution of the same volume was slowly injected to the bottom to ensure that there was a sharp interface between the two solutions. Continuous density gradients were obtained through tilted tube rotation using a gradient station with built-in programs. Then, 1.6 mL of previously prepared DNC solution was laid on the top of the as-prepared gradient solution with a 1.0 mL BD syringe (Becton, Dickinson and Company) and a disposable Pasteur

pipette (Fisher Scientific) and the tube was balanced before being placed in the ultracentrifuge. The centrifuge process was carried out at the speed of 20 000 rpm for 30 min. Finally, fractions were collected with a six-piston fractionator. For further characterization and application, the collected fractions were rinsed several times by centrifuging and replacing the solvent with MilliQ water until the density of the final disposed water (measured by a Density Meter, DMA 35) was equal to that of pure water.

Structural characterization

A high-resolution transmission electron microscope (HRTEM; Titan G2 80-200, FEI Co.) was utilized to investigate the sizes and structures of the primary particles. Aqueous solutions of DNCs were dried on 300 mesh Au grids (Ted Pella Inc., USA) and characterized with an acceleration voltage of 300 kV. The particle size histograms were obtained by counting over 150 particles per sample.

We used X-ray diffraction (XRD; Bruker D8 Advance, Cu λKα1 = 1.5406 Å, increment: 0.1 degree per step, scan speed: 1 second per step) to study the phase purity of the DNCs.

Diamond film preparation and He^+ implantation

DNC fractions in a water suspension were deposited on silicon substrates by spincoating at 2000 rpm. To promote adhesion of the DNCs, the substrate was pre-treated with a 2% solution of aminopropyltriethoxysilane (APTES) in ethanol for two minutes, rinsed in water, and heated at 100 °C for 30 minutes. DNCs deposited in this way formed uniformly dispersed monolayer films with minimal aggregation. The DNC density was determined from scanning electron micrographs (SMEs) of the films. Using Image J software, the diamond filling fraction on the underlying substrate was calculated by converting the SEM images into binary black and white using a manually set intensity threshold. The number of DNCs per unit area was determined assuming a square footprint and knowledge of the average size measured from the TEM images.

DNC films were irradiated with 20 keV He^+ at a dose of 5.9×1012 ions per cm^2 using a commercial implantation service (Innovion, San Jose CA). The irradiated DNCs were annealed at 800 °C for two hours at a pressure of 7×10^{-7} Torr, followed by thermal oxidation at 465 °C for 30 minutes in 100% oxygen at atmospheric pressure. Freely available stopping range in matter (SRIM) software was used to estimate the ion implantation range and concentration of generated vacancies.[39]

Optical characterization

DNC films were characterized using a home-built confocal microscope. A 532 nm diode pumped solid-state laser was focused onto the samples with an air immersion objective (Olympus LUCPlanFLN 40× 0.6 NA), and a steerable mirror (Newport) scanned both the laser and the emitted light. Fluorescence was passed through a dichroic mirror, bandpass filtered (650–800 nm), and coupled to a single-mode optical fiber, which served as the confocal pinhole. Avalanche photo diodes (APD, Perkin Elmer) were used for photo detection and photon statistics. Emission spectra were measured with a grating spectrometer (Jobin Yvon iHR550, 76 mm × 76 mm monochromator with 150 g mm^{-1} grating) and a CCD camera. Extended data acquisition times (30–60 seconds) for spectral measurements increased the frequency of noise originating from cosmic rays. The resulting single point peaks in the spectra were not filtered from the raw data because they were distinct from the much broader emission lines of NV centers.

Photon autocorrelation functions of single NV centers were measured to determine the luminescence intensity of NVs on our microscope. Fluorescence emissions were split into two channels using a beam splitter and detected with separate avalanche photodiodes in the Hanbury Brown and Twiss configurations. Photon coincidence in each channel as a function of the delay time was analyzed with a time-correlated single photon counting module (Picoharp). The raw coincidence counts, $c(t)$, were normalized to the coincidence rate at long delay times (where single emitters are equivalent to a Poisson-distributed source) using the formula $C_N(t) = c(t)/N_1N_2wT$, where N is the detected photon count rate in channels 1 and 2, w is the time bin size, and T is the total acquisition time. Background correction accounting for APD dark counts and non-NV luminescence gave the autocorrelation function $g^{(2)}(t) = [C_N(t) - (1 - \rho^2)]/\rho^2$, where $\rho = S/(S + B)$ is the signal- (S) to-background (B) ratio. The number of NV centers, N, was calculated from the contrast in $g^{(2)}$ at zero lag time according to $N = 1/(1 - g^{(2)}(0))$.

Conflict of interest

The authors declare no competing financial interests.

Acknowledgements

The authors acknowledge the financial support of the Office of Competitive Research Funds (OCRF) at King Abdullah University of Science and Technology (KAUST) under the "Competitive Research Grant" (CRG) program no. FIC/2010/02. ML and DLF also acknowledge support from the Schlumberger-Doll Research Center.

Notes and references

1 I. Aharonovich, A. D. Greentree and S. Prawer, *Nat. Photonics*, 2011, **5**, 397–405.
2 T. Sharda, M. Rahaman, Y. Nukaya, T. Soga, T. Jimbo and M. Umeno, *Diamond Relat. Mater.*, 2001, **10**, 561–567.
3 L. Pham, N. Bar-Gill, D. Le Sage, C. Belthangady, A. Stacey, M. Markham, D. Twitchen, M. Lukin and R. Walsworth, *Phys. Rev. B: Condens. Matter Mater. Phys.*, 2012, **86**, 121202.
4 H. Mamin, M. Kim, M. Sherwood, C. Rettner, K. Ohno, D. Awschalom and D. Rugar, *Science*, 2013, **339**, 557–560.
5 N. D. Lai, O. Faklaris, D. Zheng, V. Jacques, H.-C. Chang, J.-F. Roch and F. Treussart, *New J. Phys.*, 2013, **15**, 033030.
6 P. Maurer, J. Maze, P. Stanwix, L. Jiang, A. Gorshkov, A. A. Zibrov, B. Harke, J. Hodges, A. S. Zibrov and A. Yacoby, *Nat. Phys.*, 2010, **6**, 912–918.
7 A. S. Barnard, *Analyst*, 2009, **134**, 1751–1764.

8 L. P. McGuinness, Y. Yan, A. Stacey, D. A. Simpson, L. T. Hall, D. Maclaurin, S. Prawer, P. Mulvaney, J. Wrachtrup, F. Caruso, R. E. Scholten and L. C. L. Hollenberg, *Quantum Electronics Conference & Lasers and Electro-Optics (CLEO/IQEC/PACIFIC RIM)*, 2011, vol. 2011, pp. 601–602.
9 G. Balasubramanian, I. Chan, R. Kolesov, M. Al-Hmoud, J. Tisler, C. Shin, C. Kim, A. Wojcik, P. R. Hemmer and A. Krueger, *Nature*, 2008, **455**, 648–651.
10 P. Neumann, R. Kolesov, B. Naydenov, J. Beck, F. Rempp, M. Steiner, V. Jacques, G. Balasubramanian, M. Markham and D. Twitchen, *Nat. Phys.*, 2010, **6**, 249–253.
11 B. Hausmann, J. Choy, T. Babinec, B. Shields, I. Bulu, M. Lukin and M. Lončar, *Phys. Status Solidi A*, 2012, **209**, 1619–1630.
12 B. J. Hausmann, B. Shields, Q. Quan, P. Maletinsky, M. McCutcheon, J. T. Choy, T. M. Babinec, A. Kubanek, A. Yacoby and M. D. Lukin, *Nano Lett.*, 2012, **12**, 1578–1582.
13 T. Staudacher, F. Shi, S. Pezzagna, J. Meijer, J. Du, C. Meriles, F. Reinhard and J. Wrachtrup, *Science*, 2013, **339**, 561–563.
14 N. Mizuochi, T. Makino, H. Kato, D. Takeuchi, M. Ogura, H. Okushi, M. Nothaft, P. Neumann, A. Gali and F. Jelezko, *Nat. Photonics*, 2012, **6**, 299–303.
15 B. Grotz, M. V. Hauf, M. Dankerl, B. Naydenov, S. Pezzagna, J. Meijer, F. Jelezko, J. Wrachtrup, M. Stutzmann and F. Reinhard, *Nat. Commun.*, 2012, **3**, 729.
16 S. Pezzagna, D. Rogalla, D. Wildanger, J. Meijer and A. Zaitsev, *New J. Phys.*, 2011, **13**, 035024.
17 S. Pezzagna, D. Rogalla, H. W. Becker, I. Jakobi, F. Dolde, B. Naydenov, J. Wrachtrup, F. Jelezko, C. Trautmann and J. Meijer, *Phys. Status Solidi A*, 2011, **208**, 2017–2022.
18 Y.-R. Chang, H.-Y. Lee, K. Chen, C.-C. Chang, D.-S. Tsai, C.-C. Fu, T.-S. Lim, Y.-K. Tzeng, C.-Y. Fang and C.-C. Han, *Nat. Nanotechnol.*, 2008, **3**, 284–288.
19 Y. Morita, T. Takimoto, H. Yamanaka, K. Kumekawa, S. Morino, S. Aonuma, T. Kimura and N. Komatsu, *Small*, 2008, **4**, 2154–2157.
20 N. Mohan, Y. K. Tzeng, L. Yang, Y. Y. Chen, Y. Y. Hui, C. Y. Fang and H. C. Chang, *Adv. Mater.*, 2010, **22**, 843–847.
21 O. Faklaris, V. Joshi, T. Irinopoulou, P. Tauc, M. Sennour, H. Girard, C. l. Gesset, J.-C. Arnault, A. Thorel and J.-P. Boudou, *ACS Nano*, 2009, **3**, 3955–3962.
22 S. Vial, C. Mansuy, S. Sagan, T. Irinopoulou, F. Burlina, J. P. Boudou, G. Chassaing and S. Lavielle, *ChemBioChem*, 2008, **9**, 2113–2119.
23 T. Takimoto, T. Chano, S. Shimizu, H. Okabe, M. Ito, M. Morita, T. Kimura, T. Inubushi and N. Komatsu, *Chem. Mater.*, 2010, **22**, 3462–3471.
24 V. Vaijayanthimala and H. Chang, *Nanomedicine*, 2009, **4**, 47–55.
25 M. R. Jones, K. D. Osberg, R. J. Macfarlane, M. R. Langille and C. A. Mirkin, *Chem. Rev.*, 2011, **111**, 3736–3827.
26 J. Rabeau, A. Stacey, A. Rabeau, S. Prawer, F. Jelezko, I. Mirza and J. Wrachtrup, *Nano Lett.*, 2007, **7**, 3433–3437.
27 C. Bradac, T. Gaebel, N. Naidoo, J. R. Rabeau and A. S. Barnard, *Nano Lett.*, 2009, **9**, 3555–3564.
28 B. R. Smith, D. W. Inglis, B. Sandnes, J. R. Rabeau, A. V. Zvyagin, D. Gruber, C. J. Noble, R. Vogel, E. Ōsawa and T. Plakhotnik, *Small*, 2009, **5**, 1649–1653.
29 V. N. Mochalin, O. Shenderova, D. Ho and Y. Gogotsi, *Nat. Nanotechnol.*, 2011, **7**, 11–23.
30 J.-P. Boudou, P. A. Curmi, F. Jelezko, J. Wrachtrup, P. Aubert, M. Sennour, G. Balasubramanian, R. Reuter, A. Thorel and E. Gaffet, *Nanotechnology*, 2009, **20**, 235602.
31 N. Komatsu and F. Wang, *Materials*, 2010, **3**, 3818–3844.
32 M. C. Hersam, *Nat. Nanotechnol.*, 2008, **3**, 387–394.
33 W. Peng, R. Mahfouz, J. Pan, Y. Hou, P. M. Beaujuge and O. M. Bakr, *Nanoscale*, 2013, **5**, 5017–5026.
34 A. Pentecost, S. Gour, V. Mochalin, I. Knoke and Y. Gogotsi, *ACS Appl. Mater. Interfaces*, 2010, **2**, 3289–3294.
35 S. Ghosh, S. M. Bachilo and R. B. Weisman, *Nat. Nanotechnol.*, 2010, **5**, 443–450.
36 D. Steinigeweg, M. Schütz, M. Salehi and S. Schlücker, *Small*, 2011, **7**, 2443–2448.
37 I. Larionova, V. Kuznetsov, A. Frolov, O. Shenderova, S. Moseenkov and I. Mazov, *Diamond Relat. Mater.*, 2006, **15**, 1804–1808.
38 L. Bai, X. Ma, J. Liu, X. Sun, D. Zhao and D. G. Evans, *J. Am. Chem. Soc.*, 2010, **132**, 2333–2337.
39 J. F. Ziegler, M. Ziegler and J. Biersack, *Nucl. Instrum. Methods Phys. Res., Sect. B*, 2010, **268**, 1818–1823.
40 R. Brouri, A. Beveratos, J.-P. Poizat and P. Grangier, *Opt. Lett.*, 2000, **25**, 1294–1296.
41 C. Bradac, T. Gaebel, N. Naidoo, M. Sellars, J. Twamley, L. Brown, A. Barnard, T. Plakhotnik, A. Zvyagin and J. Rabeau, *Nat. Nanotechnol.*, 2010, **5**, 345–349.
42 F. Waldermann, P. Olivero, J. Nunn, K. Surmacz, Z. Wang, D. Jaksch, R. Taylor, I. Walmsley, M. Draganski and P. Reichart, *Diamond Relat. Mater.*, 2007, **16**, 1887–1895.
43 Y. Y. Hui, Y.-R. Chang, T.-S. Lim, H.-Y. Lee, W. Fann and H.-C. Chang, *Appl. Phys. Lett.*, 2009, **94**, 013104.
44 L.-H. Chen, T.-S. Lim and H.-C. Chang, *J. Opt. Soc. Am. B*, 2012, **29**, 2309–2313.

